



**Prediction of Swerving Motion of a Dual-Spin Projectile
With Lateral Pulsejets in Atmospheric Flight**

by Bradley Burchett, Allen Peterson, and Mark Costello

ARL-CR-570

November 2005

prepared by

**Oregon State University
Corvallis, OR 97331-6001**

under contract

W911QX-04-P0270

NOTICES

Disclaimers

The findings in this report are not to be construed as an official Department of the Army position unless so designated by other authorized documents.

Citation of manufacturer's or trade names does not constitute an official endorsement or approval of the use thereof.

Destroy this report when it is no longer needed. Do not return it to the originator.

Army Research Laboratory

Aberdeen Proving Ground, MD 21005-5066

ARL-CR-570

November 2005

Prediction of Swerving Motion of a Dual-Spin Projectile With Lateral Pulsejets in Atmospheric Flight

**Bradley Burchett, Allen Peterson, and Mark Costello
Oregon State University**

prepared by

**Oregon State University
Corvallis, OR 97331-6001**

under contract

W911QX-04-P0270

REPORT DOCUMENTATION PAGE			<i>Form Approved</i> OMB No. 0704-0188	
Public reporting burden for this collection of information is estimated to average 1 hour per response, including the time for reviewing instructions, searching existing data sources, gathering and maintaining the data needed, and completing and reviewing the collection information. Send comments regarding this burden estimate or any other aspect of this collection of information, including suggestions for reducing the burden, to Department of Defense, Washington Headquarters Services, Directorate for Information Operations and Reports (0704-0188), 1215 Jefferson Davis Highway, Suite 1204, Arlington, VA 22202-4302. Respondents should be aware that notwithstanding any other provision of law, no person shall be subject to any penalty for failing to comply with a collection of information if it does not display a currently valid OMB control number. PLEASE DO NOT RETURN YOUR FORM TO THE ABOVE ADDRESS.				
1. REPORT DATE (DD-MM-YYYY) November 2005		2. REPORT TYPE Final		3. DATES COVERED (From - To) October 2004–October 2005
4. TITLE AND SUBTITLE Prediction of Swerving Motion of a Dual-Spin Projectile With Lateral Pulsejets in Atmospheric Flight			5a. CONTRACT NUMBER W911QX-04-P0270	
			5b. GRANT NUMBER	
			5c. PROGRAM ELEMENT NUMBER	
6. AUTHOR(S) Bradley Burchett, Allen Peterson, and Mark Costello			5d. PROJECT NUMBER 622618.H80	
			5e. TASK NUMBER	
			5f. WORK UNIT NUMBER	
7. PERFORMING ORGANIZATION NAME(S) AND ADDRESS(ES) Oregon State University Corvallis, OR 97331-6001			8. PERFORMING ORGANIZATION REPORT NUMBER	
9. SPONSORING/MONITORING AGENCY NAME(S) AND ADDRESS(ES) U.S. Army Research Laboratory ATTN: AMSRD-ARL-WM-BC Aberdeen Proving Ground, MD 21005-5066			10. SPONSOR/MONITOR'S ACRONYM(S)	
			11. SPONSOR/MONITOR'S REPORT NUMBER(S) ARL-CR-570	
12. DISTRIBUTION/AVAILABILITY STATEMENT Approved for public release; distribution is unlimited.				
13. SUPPLEMENTARY NOTES Point of contact for this report is Peter Plostins, U.S. Army Research Laboratory, ATTN: AMSRD-ARL-WM-BC, Aberdeen Proving Ground, MD 21005-5066				
14. ABSTRACT Using the linear theory for a dual-spin projectile in atmospheric flight, closed form expressions were obtained for swerving motion under the action of lateral pulsejets. Trajectory results generated by the linear theory equations and a fully nonlinear seven degree-of-freedom dual-spin projectile model agreed favorably. The analytic solution provided a relatively straight forward and computationally efficient means of trajectory estimation which is useful within smart weapon flight control systems. In order to accurately predict the impact point using the analytic solution, the dual-spin projectile linear model must be updated periodically. Terminal impact point prediction degrades rapidly as the linear model update interval is increased beyond a critical value. Control authority, as defined by the change in impact location due to a pulsejet firing, steadily decreases as a function of projectile down range position.				
15. SUBJECT TERMS dual-spin projectile, pulsejet control, linear theory, lateral pulse jets, guidance navigation and control				
16. SECURITY CLASSIFICATION OF:			17. LIMITATION OF ABSTRACT UL	18. NUMBER OF PAGES 30
a. REPORT UNCLASSIFIED	b. ABSTRACT UNCLASSIFIED	c. THIS PAGE UNCLASSIFIED		
			19b. TELEPHONE NUMBER (Include area code) 410-278-8878	

Contents

List of Figures	iv
List of Tables	iv
1. Introduction	1
2. Dual-Spin Projectile Dynamic Model	2
3. Analytic Solution	5
4. Pulsejet Force and Moment Conditions	10
5. Results	10
6. Conclusions	16
7. References	17
Appendix. Dual-Spin Linear Theory Coefficients	19
List of Symbols, Abbreviations, and Acronyms	21
Distribution List	23

List of Figures

Figure 1. Projectile position coordinate definitions.	2
Figure 2. Projectile orientation definitions.	3
Figure 3. Cross range vs. range.	12
Figure 4. Altitude vs. range.	12
Figure 5. Pitch angle vs. range.	13
Figure 6. Yaw angle vs. range.	14
Figure 7. Roll rate vs. range.	14
Figure 8. Target prediction error vs. model update interval.	15
Figure 9. Induced pulsejet swerve vs. range to target.	15

List of Tables

Table 1. Projectile physical properties.	11
Table 2. Projectile state conditions.	11

1. Introduction

With clever integration of microelectromechanical sensors and actuators into new projectile configurations, future weapon systems hope to achieve a notable leap in accuracy and lethality. Because some sensors and control mechanisms require different levels of spin to operate properly, new multicomponent projectile configurations are being investigated. The dual-spin projectile configuration is one such concept that consists of forward and aft components, connected through a bearing, which roll at different rates.

A potential control mechanism for smart weapons trajectory control is a cluster of lateral pulsejets. Each pulsejet imparts a relatively short duration, yet large lateral body force on the projectile. By mounting a set of pulsejets on either the forward or aft section of a dual-spin projectile, a specific trajectory can be tracked. When designing a projectile pulsejet flight control system to minimize terminal miss distance, pulsejet firing logic relies on real-time estimation of the effect of firing a particular jet on the miss distance at an arbitrary time and system state. In theory, this can be accomplished by numerically integrating the nonlinear equations of motion from a given point to the target. However, from a practical point of view, real-time numerical integration of the nonlinear equations of motion from a given state to the target at each flight control system computation cycle represents too large a computational burden on the on-board microprocessor. Hence, computationally-efficient trajectory prediction of smart weapon projectile configurations is needed for insertion into control laws. Along these lines, Guidos and Cooper (*1*) developed closed form expressions for swerve of a rigid nonrolling projectile with a lateral pulsejet applied. Their analysis allows for finite duration impulse loads and showed that under mild conditions on spin rate, singular and finite duration impulses yield the same effect on the trajectory.

Although the dynamics of dual-spin spacecraft have been extensively studied (*2–12*), work on the atmospheric flight mechanics of dual-spin projectiles has been comparatively sparse. Smith et al. (*13*) developed a dynamic model of a dual-spin projectile and employed this model to simulate a smart artillery shell. More recently, Costello and Peterson (*14*) reported a more general dual-spin projectile dynamic model which permits asymmetric mass properties and generalized bearing friction. This model was subsequently used to develop a linear theory and stability boundaries for this configuration. The work reported here extends the dual-spin projectile linear equations to account for the effect of lateral pulsejets in the prediction of angular and swerving motion. The swerving dynamics are solved in closed form, resulting in computationally-simple algebraic expressions for the projectile trajectory under the influence of lateral pulsejets.

2. Dual-Spin Projectile Dynamic Model

The dynamic model for a dual-spin projectile admits a total of seven degrees-of-freedom, including the components of the position vector of the mass center and the Euler yaw, pitch, aft body roll, and forward body roll angles. Figures 1 and 2 provide indicate coordinates used to specify position and orientation for the dual-spin projectile dynamic model. Linear projectile theory is used to simplify the highly nonlinear dynamic equations to a set of linear ordinary differential equations. More details on projectile linear theory can be found in McCoy (15). The linear equations developed by Costello and Peterson (14) neglected gravity, since their primary interest was dynamic stability, and also did not include lateral pulsejet forces in the formulation.

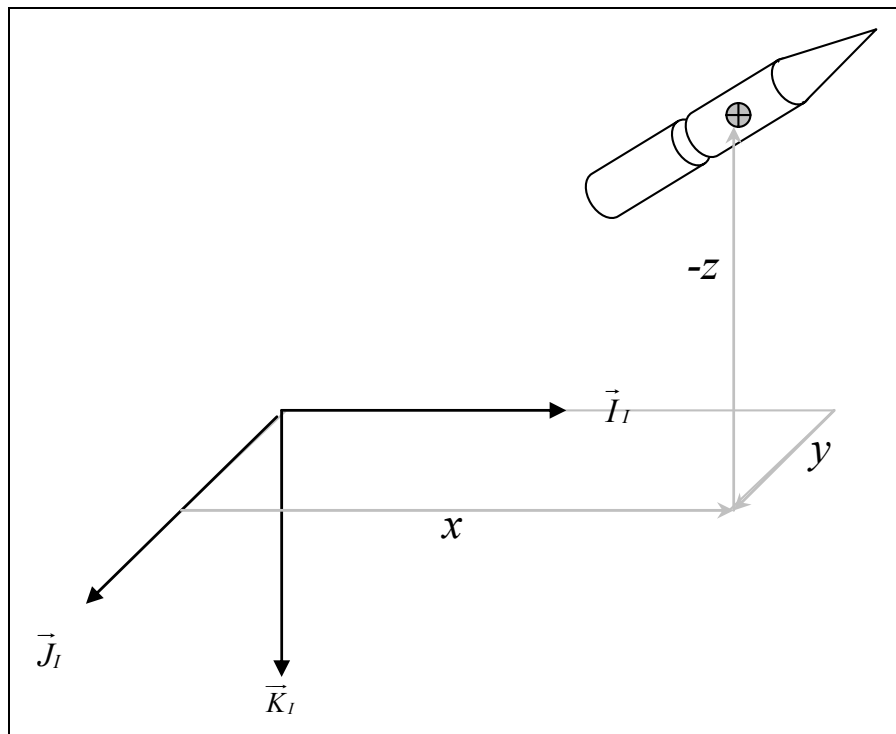


Figure 1. Projectile position coordinate definitions.

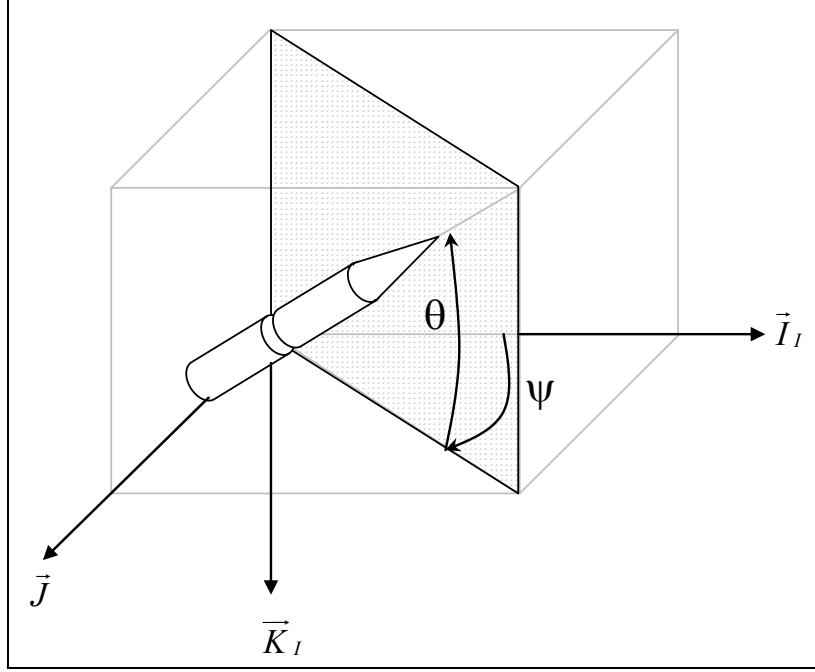


Figure 2. Projectile orientation definitions.

Equations 1–10 remove these two limitations and represent a modified set of dynamic equations describing the motion of a dual-spin projectile in atmospheric flight.

$$V' = -\frac{\rho SDC_{x0}}{2m} V \cdot \quad (1)$$

$$\phi'_F = \frac{D}{V} p_F \cdot \quad (2)$$

$$\phi'_A = \frac{D}{V} p_A \cdot \quad (3)$$

$$\begin{Bmatrix} p'_F \\ p'_A \end{Bmatrix} = \begin{bmatrix} H & J \\ T & L \end{bmatrix} \begin{Bmatrix} p_F \\ p_A \end{Bmatrix} + \begin{Bmatrix} M \\ N \end{Bmatrix} \cdot \quad (4)$$

$$\begin{Bmatrix} v' \\ w' \\ q' \\ r' \end{Bmatrix} = \begin{bmatrix} -A & 0 & 0 & -D \\ 0 & -A & D & 0 \\ B/D & C/D & E & -F \\ -C/D & B/D & F & E \end{bmatrix} \begin{Bmatrix} v \\ w \\ q \\ r \end{Bmatrix} + \begin{Bmatrix} Y_I D / (mV) \\ Dg/V + Z_I D / (mV) \\ -R_{IX} Z_I D / (VI_{YY}) \\ R_{IX} Y_I D / (VI_{YY}) \end{Bmatrix} \cdot \quad (5)$$

$$\theta' = \frac{D}{V} q \cdot \quad (6)$$

$$\psi' = \frac{D}{V} r \cdot \quad (7)$$

$$x' = D. \quad (8)$$

$$y' = \frac{D}{V}v + \psi D. \quad (9)$$

$$z' = \frac{D}{V}w - \theta D. \quad (10)$$

In equations 1–10, the ‘ symbol denotes differentiation with respect to nondimensional arc length, s . The constants used in the previous equations are defined as follows:

$$A = \left[\frac{\rho SD}{2m} \right] (C_{NA}). \quad (11)$$

$$B = \left[\frac{\rho SD}{2m} \right] \left[\frac{mD}{I_{YY}^T} \right] \left(\frac{D}{V} \right) \left((\tilde{R}_{fx} + r_{fx}) \frac{C_{NPA}^F}{2} p_F + (\tilde{R}_{ax} + r_{ax}) \frac{C_{NPA}^A}{2} p_A \right). \quad (12)$$

$$C = \left[\frac{\rho SD}{2m} \right] \left[\frac{mD}{I_{YY}^T} \right] C_{MA}. \quad (13)$$

$$E = \left[\frac{\rho SD}{2m} \right] \left[\frac{mD^2}{I_{YY}^T} \right] \frac{C_{MQ}}{2}. \quad (14)$$

$$F = \frac{D}{V} \frac{(I_{XX}^F p_F + I_{XX}^A p_A)}{I_{YY}^T}. \quad (15)$$

$$H = \frac{\rho SD^3 C_{LP}^F}{4I_{XX}^F} - \frac{DC_V}{VI_{XX}^F}. \quad (16)$$

$$J = \frac{DC_V}{VI_{XX}^F}. \quad (17)$$

$$T = \frac{DC_V}{VI_{XX}^A}. \quad (18)$$

$$L = \frac{\rho SD^3 C_{LP}^A}{4I_{XX}^A} - \frac{DC_V}{VI_{XX}^A}. \quad (19)$$

$$M = \frac{\rho SD^2 VC_{DD}^F}{2I_{xx}^F}. \quad (20)$$

$$N = \frac{\rho SD^2 VC_{DD}^A}{2I_{xx}^A}. \quad (21)$$

$$C_{MA} = (R_{fx} + r_{fx}) C_{NA}^F + (R_{ax} + r_{ax}) C_{NA}^A. \quad (22)$$

$$I_{YY}^T = I_{YY}^F + m_f r_{fx}^2 + I_{YY}^A + m_a r_{ax}^2. \quad (23)$$

The impulse force components Y_I and Z_I represent impulse forces that are applied to the projectile in the nonrolling reference frame. These loads and the associated moment arm, R_{IX} , are effective forces and moments. Due to aerodynamic interaction, the force and moment generated by the lateral pulsejets is in general different than what would be measured on a test stand. Also, for this report, the impulse forces are mathematically treated as singular impulses. The bearing coupling rolling resistance is assumed to be of the hydrodynamic type.

3. Analytic Solution

Pulsejet forces and moments that appear in equation 5 are assumed to occur over a relatively short duration of time compared to the motion of the projectile; hence, their effect is impulsive in nature. An impulsive force acting on a rigid body creates a discontinuity in the translational and rotational velocity of the body at the time of the impulse (16). To simulate motion of the projectile with pulsejets acting on the system, a piecewise solution is constructed that consists of free-flight and pulsejet discontinuity segments. Expressions for free-flight solution segments are given in this section, while the pulsejet state discontinuity conditions are provided in the next section.

As seen in equation 1, the total velocity is dynamically uncoupled from the system, but appears in a nonlinear fashion in the remaining state dynamic equations. As is customary in projectile linear theory (15), it is assumed that the total velocity changes slowly with respect to the other states of the system so it can be treated as a constant in the other dynamic equations. When viewed in this light, the equations of motion become linear and the equations of motion for angle of attack and roll motion become uncoupled.

The total velocity of the projectile exhibits exponential decay as the round flies down range. Equation 24 provides the total velocity solution:

$$V = V_0 e^{-\rho SDC X_0 s / (2m)}. \quad (24)$$

The solution to the roll rate equations is aided by first defining the decay rates, as shown in equation 25.

$$\sigma_{1,2} = \frac{H + L \pm \sqrt{H^2 - 2HL + L^2 + 4KJ}}{2}. \quad (25)$$

With the roll rate decay rate given by equation 25, the roll rate solution can be written as

$$p_F = \frac{1}{\sigma_1 - \sigma_2} \left\{ (\sigma_1 - L) \left[\left(\Gamma_{11} + \frac{1}{\sigma_1} \Gamma_{12} \right) e^{\sigma_1 s} - \frac{1}{\sigma_1} \Gamma_{12} \right] \right. \\ \left. + (\sigma_2 - L) \left[\left(\Gamma_{21} + \frac{1}{\sigma_2} \Gamma_{22} \right) e^{\sigma_2 s} - \frac{1}{\sigma_2} \Gamma_{22} \right] \right\}, \quad (26)$$

and

$$p_A = \frac{T}{\sigma_1 - \sigma_2} \left\{ \left(\Gamma_{11} + \frac{1}{\sigma_1} \Gamma_{12} \right) e^{\sigma_1 s} - \frac{1}{\sigma_1} \Gamma_{12} \right. \\ \left. + \left(\Gamma_{21} + \frac{1}{\sigma_2} \Gamma_{22} \right) e^{\sigma_2 s} - \frac{1}{\sigma_2} \Gamma_{22} \right\}, \quad (27)$$

where

$$\Gamma_{11} = T p_{F_0} + (L - \sigma_2) p_{A_0}, \quad (28)$$

$$\Gamma_{12} = TM + (L - \sigma_2) N, \quad (29)$$

$$\Gamma_{21} = T p_{F_0} + (\sigma_1 - L) p_{A_0}, \quad (30)$$

and

$$\Gamma_{22} = TM + (\sigma_1 - L) N. \quad (31)$$

As given in equation 5, the equations of motion for epicyclic pitching and yawing behavior consists of coupled motion of v , w , q , and r . The slow and fast modes of the epicyclic dynamic equations are given by equations 32 and 33:

$$\lambda_F = \sigma_F + i\phi_F \quad (32)$$

and

$$\lambda_S = \sigma_S + i\phi_S, \quad (33)$$

where

$$\sigma_F = \frac{-(A - E)}{2} \left[1 + \frac{F}{\sqrt{F^2 - 4C}} \left(1 - \frac{(2AF + 2B)}{F(A - E)} \right) \right], \quad (34)$$

$$\sigma_S = \frac{-(A - E)}{2} \left[1 - \frac{F}{\sqrt{F^2 - 4C}} \left(1 - \frac{(2AF + 2B)}{F(A - E)} \right) \right], \quad (35)$$

$$\phi_F = \frac{1}{2} \left[F + \sqrt{F^2 - 4C} \right], \quad (36)$$

and

$$\phi_s = \frac{1}{2} \left[F - \sqrt{F^2 - 4C} \right]. \quad (37)$$

Corresponding to the modes given in equations 32 and 33, the right and left Eigenvector matrices are given by equations 38 and 39, respectively.

$$\begin{bmatrix} \xi_1^T \\ \xi_2^T \\ \xi_1^{T*} \\ \xi_2^{T*} \end{bmatrix} = \begin{bmatrix} i & i & -i & -i \\ 1 & 1 & 1 & 1 \\ \frac{K + \sqrt{Q}}{2D} & \frac{K - \sqrt{Q}}{2D} & \frac{R + \sqrt{S}}{2D} & \frac{R - \sqrt{S}}{2D} \\ -\frac{i(K + \sqrt{Q})}{2D} & -\frac{i(K - \sqrt{Q})}{2D} & \frac{i(R + \sqrt{S})}{2D} & \frac{i(R - \sqrt{S})}{2D} \end{bmatrix}. \quad (38)$$

$$\begin{bmatrix} \eta_1^T \\ \eta_2^T \\ \eta_1^{T*} \\ \eta_2^{T*} \end{bmatrix} = \frac{1}{2} \begin{bmatrix} \frac{iv}{(-v + \mu)} & \frac{-v}{(-v + \mu)} & \frac{1}{(-v + \mu)} & \frac{i}{(-v + \mu)} \\ \frac{-i\mu}{(-v + \mu)} & \frac{-\mu}{(-v + \mu)} & \frac{-1}{(-v + \mu)} & \frac{-i}{(-v + \mu)} \\ \frac{iv^*}{(v^* - \mu^*)} & \frac{v^*}{(v^* - \mu^*)} & \frac{-1}{(v^* - \mu^*)} & \frac{i}{(v^* - \mu^*)} \\ \frac{-i\mu^*}{(v^* - \mu^*)} & \frac{-\mu^*}{(v^* - \mu^*)} & \frac{1}{(v^* - \mu^*)} & \frac{-i}{(v^* - \mu^*)} \end{bmatrix}. \quad (39)$$

The constants utilized in equations 38 and 39 are defined as follows. Note that the * symbol denotes complex conjugate.

$$K = (E - A) + 2A + iF, \quad (40)$$

$$Q = (E - A)^2 + 4AE + 4C - F^2 + 2i(F(E - A) + 2(AF + B)), \quad (41)$$

$$R = (E - A) + 2A - iF, \quad (42)$$

$$S = (E - A)^2 + 4AE + 4C - F^2 - 2i(F(E - A) + 2(AF + B)), \quad (43)$$

$$v = \frac{(K + \sqrt{Q})}{2D}, \quad (44)$$

and

$$\mu = \frac{(K - \sqrt{Q})}{2D}. \quad (45)$$

The vector χ , which represents the initial conditions with the steady state portion removed, is used to define the homogeneous response of the epicyclic equations.

$$\chi = \begin{Bmatrix} v_0 \\ w_0 \\ q_0 \\ r_0 \end{Bmatrix} - \begin{bmatrix} -A & 0 & 0 & -D \\ 0 & -A & D & 0 \\ B/D & C/D & E & -F \\ -C/D & B/D & F & E \end{bmatrix}^{-1} \begin{Bmatrix} 0 \\ Dg/V \\ 0 \\ 0 \end{Bmatrix}. \quad (46)$$

Using the definitions provided by equations 38, 39, and 46, the homogeneous solution for each epicyclic state variable is expressed as a combination of the fast and slow modes.

$$v_H = \Omega_{vF} e^{\sigma_{FS}} \sin(\phi_F s + \theta_{vF}) + \Omega_{vS} e^{\sigma_{SS}} \sin(\phi_S s + \theta_{vS}), \quad (47)$$

$$w_H = \Omega_{wF} e^{\sigma_{FS}} \sin(\phi_F s + \theta_{wF}) + \Omega_{wS} e^{\sigma_{SS}} \sin(\phi_S s + \theta_{wS}), \quad (48)$$

$$q_H = \Omega_{qF} e^{\sigma_{FS}} \sin(\phi_F s + \theta_{qF}) + \Omega_{qS} e^{\sigma_{SS}} \sin(\phi_S s + \theta_{qS}), \quad (49)$$

and

$$r_H = \Omega_{rF} e^{\sigma_{FS}} \sin(\phi_F s + \theta_{rF}) + \Omega_{rS} e^{\sigma_{SS}} \sin(\phi_S s + \theta_{rS}), \quad (50)$$

while the particular solution is given by equation 51.

$$\begin{Bmatrix} v_P \\ w_P \\ q_P \\ r_P \end{Bmatrix} = - \begin{bmatrix} -A & 0 & 0 & -D \\ 0 & -A & D & 0 \\ B/D & C/D & E & -F \\ -C/D & B/D & F & E \end{bmatrix}^{-1} \begin{Bmatrix} 0 \\ Dg/V \\ 0 \\ 0 \end{Bmatrix}. \quad (51)$$

Expressions for the modal amplitudes and phase angles used in equations 47–50 are provided in the appendix. The total epicyclic solution is the summation of the homogeneous and particular solutions.

$$\begin{Bmatrix} v \\ w \\ q \\ r \end{Bmatrix} = \begin{Bmatrix} v_H \\ w_H \\ q_H \\ r_H \end{Bmatrix} + \begin{Bmatrix} v_P \\ w_P \\ q_P \\ r_P \end{Bmatrix}. \quad (52)$$

The solutions for the Euler pitch and yaw angles are obtained by integrating the solutions for the pitch rate and yaw rate, respectively.

$$\begin{aligned}
\psi = & \psi_0 + \frac{D}{V}(r_p s) \\
& + \frac{D}{V} \left(\frac{-\phi_F}{\beta_F} \left[e^{\sigma_F s} \cos(\phi_F s + \theta_{rF}) - \cos \theta_{rF} \right] + \frac{\sigma_F}{\beta_F} \left[e^{\sigma_F s} \sin(\phi_F s + \theta_{rF}) - \sin \theta_{rF} \right] \right) \Omega_{rF} \\
& + \frac{D}{V} \left(\frac{-\phi_S}{\beta_S} \left[e^{\sigma_S s} \cos(\phi_S s + \theta_{rS}) - \cos \theta_{rS} \right] + \frac{\sigma_S}{\beta_S} \left[e^{\sigma_S s} \sin(\phi_S s + \theta_{rS}) - \sin \theta_{rS} \right] \right) \Omega_{rS}, \quad (53)
\end{aligned}$$

and

$$\begin{aligned}
\theta = & \theta_0 + \frac{D}{V}(q_p s) \\
& + \frac{D}{V} \left(\frac{-\phi_F}{\beta_F} \left[e^{\sigma_F s} \cos(\phi_F s + \theta_{qF}) - \cos \theta_{qF} \right] + \frac{\sigma_F}{\beta_F} \left[e^{\sigma_F s} \sin(\phi_F s + \theta_{qF}) - \sin \theta_{qF} \right] \right) \Omega_{qF} \\
& + \frac{D}{V} \left(\frac{-\phi_S}{\beta_S} \left[e^{\sigma_S s} \cos(\phi_S s + \theta_{qS}) - \cos \theta_{qS} \right] + \frac{\sigma_S}{\beta_S} \left[e^{\sigma_S s} \sin(\phi_S s + \theta_{qS}) - \sin \theta_{qS} \right] \right) \Omega_{qS}, \quad (54)
\end{aligned}$$

where

$$\beta_F = \sigma_F^2 + \phi_F^2 \quad (55)$$

and

$$\beta_S = \sigma_S^2 + \phi_S^2. \quad (56)$$

The trajectory or swerve solution is then obtained by substituting equations 47, 48, and 49 into equations 9 and 10 and subsequently integrating. The final results are given by equations 57 and 58.

$$\begin{aligned}
\frac{y}{D} = & \frac{y_0}{D} + \left(\psi_0 + \frac{v_0}{V_0} \right) s \\
& + \left[\frac{\rho SD}{2m} \right] \frac{(C_{X0} - C_{NA})}{V_0} \left(\frac{\Omega_{vF}}{\phi_F^2} \left(e^{\sigma_F^* s} \sin(\phi_F s + \theta_{vF} - \pi) - \sin(\theta_{vF} - \pi) - \phi_F \cos(\theta_{vF} - \pi) s \right) \right) \\
& + \left[\frac{\rho SD}{2m} \right] \frac{(C_{X0} - C_{NA})}{V_0} \left(\frac{\Omega_{vS}}{\phi_S^2} \left(e^{\sigma_S^* s} \sin(\phi_S s + \theta_{vS} - \pi) - \sin(\theta_{vS} - \pi) - \phi_S \cos(\theta_{vS} - \pi) s \right) \right). \quad (57)
\end{aligned}$$

$$\begin{aligned}
\frac{z}{D} = & \frac{z_0}{D} + \left(-\theta_0 + \frac{w_0}{V_0} \right) s + g \left(\frac{mD}{\rho SDC_{X0}} \right)^2 \left(e^{\frac{\rho SD}{m} C_{X0} s} - \frac{\rho SD}{m} C_{X0} s - 1 \right) \\
& + \left[\frac{\rho SD}{2m} \right] \frac{(C_{X0} - C_{NA})}{V_0} \left(\frac{\Omega_{wF}}{\phi_F^2} \left(e^{\sigma_F^* s} \sin(\phi_F s + \theta_{wF} - \pi) - \sin(\theta_{wF} - \pi) - \phi_F \cos(\theta_{wF} - \pi) s \right) \right) \\
& + \left[\frac{\rho SD}{2m} \right] \frac{(C_{X0} - C_{NA})}{V_0} \left(\frac{\Omega_{wS}}{\phi_S^2} \left(e^{\sigma_S^* s} \sin(\phi_S s + \theta_{wS} - \pi) - \sin(\theta_{wS} - \pi) - \phi_S \cos(\theta_{wS} - \pi) s \right) \right). \quad (58)
\end{aligned}$$

Equations 57 and 58 provide relatively simple expressions for the altitude and cross range of a dual-spin projectile as a function of range. Both the cross range and altitude solutions contain

constant, linear, and oscillatory terms. The altitude formula has an additional parabolic term to account for trajectory bending due to gravity.

4. Pulsejet Force and Moment Conditions

The net effect of a pulsejet force is a discontinuity in the translational and rotational velocity of the body at the time of the impulse. The discontinuity conditions are found by transforming equation 5 to the Laplace domain and noting the additional impulse terms adding with the pre-impulse initial conditions. The results are given by equations 59–62.

$$v_0^+ = v_0^- + \frac{Y_I D}{mV}. \quad (59)$$

$$w_0^+ = w_0^- + \frac{Z_I D}{mV}. \quad (60)$$

$$q_0^+ = q_0^- - \frac{R_{IX} Z_I D}{I_{YY} V}. \quad (61)$$

$$r_0^+ = r_0^- + \frac{R_{IX} Y_I D}{I_{YY} V}. \quad (62)$$

In equations 52–55, the superscript “+” denotes after impulse and the superscript “–” denotes before impulse. Since the epicyclic solution amplitude and phase angles (Ω_{vF} , Ω_{vS} , Ω_{wF} , Ω_{wS} , Ω_{qF} , Ω_{qS} , Ω_{rF} , Ω_{rS} , θ_{vF} , θ_{vS} , θ_{wF} , θ_{wS} , θ_{qF} , θ_{qS} , θ_{rF} , and θ_{rS}) all depend on v_0 , w_0 , q_0 , and $r_0 - \chi$, the dynamic model must be updated at s^+ to accurately account for the discontinuity in the epicyclic solution formulas.

5. Results

In order to investigate the utility of the simple trajectory formulas derived previously, the results that follow compare the trajectory of a dual-spin projectile computed by numerically integrating the fully nonlinear equations of motion (13) with the linear theory analytical solution. The numerical solution was generated using a fixed step fourth-order Runge Kutta algorithm with a time step of 0.00001 s. Tables 1 and 2 list the physical parameters and state conditions for the projectile considered in trajectory comparison. The linear model is updated for each change in range of one caliber. In all cases, the numerical nonlinear simulation and the analytic closed form solution are in agreement. Figures 3 and 4 show the swerve of the projectile. A difference of approximately 10 ft between the numerical nonlinear solution and the analytic solution at a

Table 1. Projectile physical properties.

Parameter	Value
Projectile length	4.5 ft
Projectile reference diameter	0.23 ft
Projectile weight	15.9 lb
Composite body mass center location	2.81 ft (from base)
Forward body mass center location	3.85 ft (from base)
Aft body mass center location	1.35 ft (from base)
Forward body roll inertia	0.0022 slug ft ²
Forward body pitch inertia	0.019 slug ft ²
Aft body roll inertia	0.002 slug ft ²
Aft body pitch inertia	0.42 slug ft ²
Bearing location	3.18 ft (from base)
Bearing viscous damping coefficient	0.0001
Lateral pulsejet stationline location	3.8 ft (from base)
Lateral pulsejet butto line location	0.12 ft
Lateral pulsejet waterline location	0.0 ft

Table 2. Projectile state conditions.

State Variable	Initial	Before Pulse	After Pulse
x	0.0 ft	419.0 ft	419.0 ft
y	-0.76 ft	-1.0 ft	-1.0 ft
z	-287.0 ft	-375.0 ft	-375.0 ft
ϕ_F	4.6°	5.8°	5.8°
ϕ_A	168.1°	156.5°	156.5°
θ	0.2°	0.2°	0.2°
ψ	-0.0007°	0.0006°	0.0006°
V	2497.0 ft/s	2420.0 ft/s	2420.0 ft/s
v	0.17 ft/s	-0.1 ft/s	1.8 ft/s
w	-0.64 ft/s	0.4 ft/s	-0.9 ft/s
p_F	7.3 rad/s	6.7 rad/s	6.7 rad/s
p_A	-10.1 rad/s	-83.8 rad/s	-83.8 rad/s
q	-0.006 rad/s	-0.01 rad/s	2.14 rad/s
r	0.001 rad/s	0.0004 rad/s	3.04 rad/s

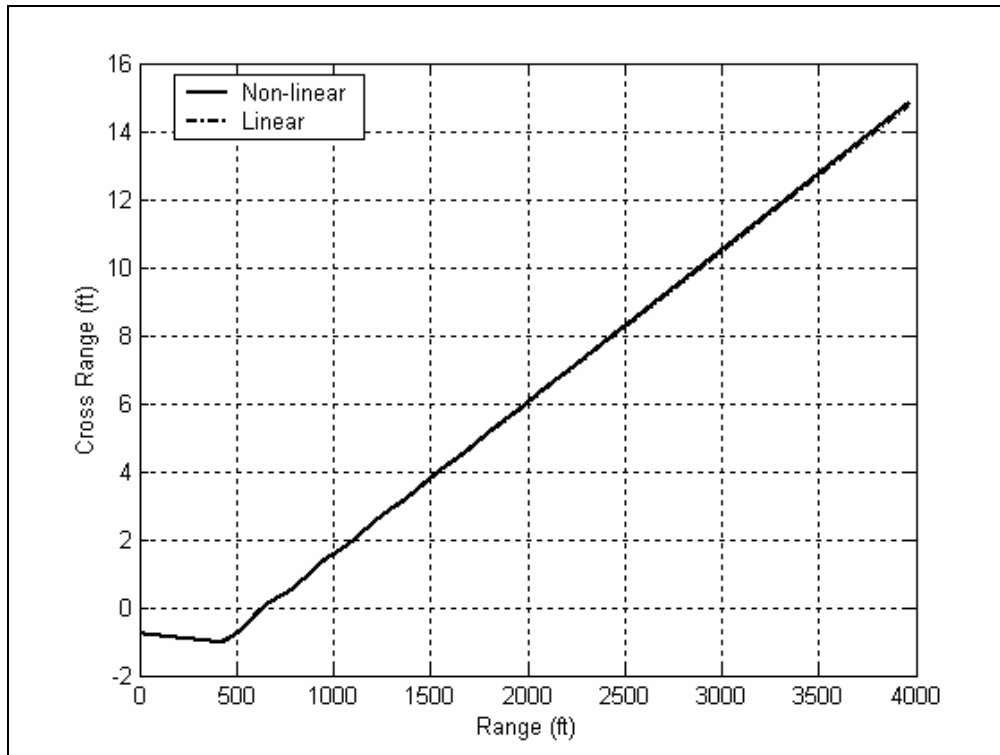


Figure 3. Cross range vs. range.

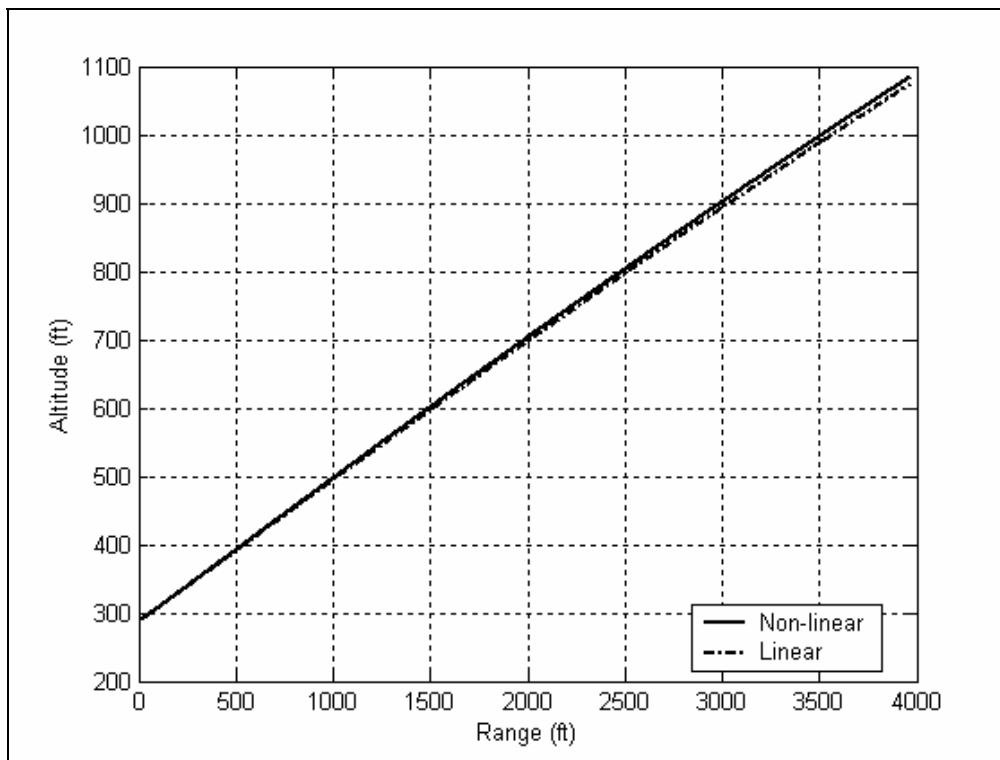


Figure 4. Altitude vs. range.

range of 3750 ft is apparent in the altitude trace. When viewed from the rear, the projectile drifts slightly to the left prior to the pulsejet firing. After the pulsejet is fired, the pulsejet turns and drifts to the right. Toward the end of the trajectory, the lateral pulsejet has changed the cross range impact point by approximately 17 ft. Figures 5 and 6 show that the action of the pulsejet induces Euler angle changes exceeding 5° . Because of the roll orientation when the pulsejet was fired, the altitude response does not show an effect from the pulsejet. The fins mounted on the aft body along with inherent roll damping combine to create the aft body roll rate history shown in figure 7. The forward body roll rate history is driven by the viscous friction in the bearing and the roll rate of the aft body. Figure 8 displays the difference in the predicted impact point of the numerical nonlinear simulation and the analytic solution as a function of the linear model update interval. At the range of 3750 ft, the impact error prediction is below 10 ft. Updating the linear model used for the analytical solution beyond 4000 cal of travel results in significant increase in impact point error. Figure 9 examines the potential change in impact point location as a function of down range position. After the epicyclic dynamics have settled, the swerve solution is dominated by the linear term. Firing a pulsejet changes the slope of the linear term. As the projectile closes on the target, the potential change in position of the round at the target due to firing a lateral pulsejet decreases, since a reduced distance to the target reduces the linear swerve changes at the target. Defining control authority as the potential change in swerve at the target, the control authority of a lateral pulsejet decreases as the projectile travels down range.

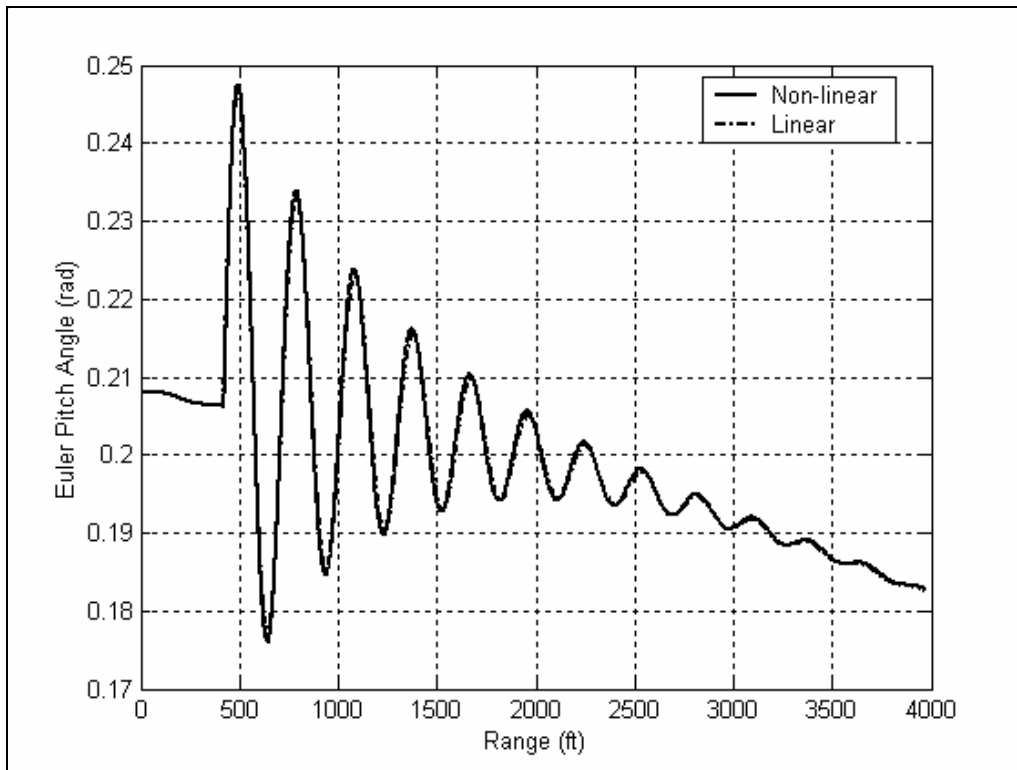


Figure 5. Pitch angle vs. range.

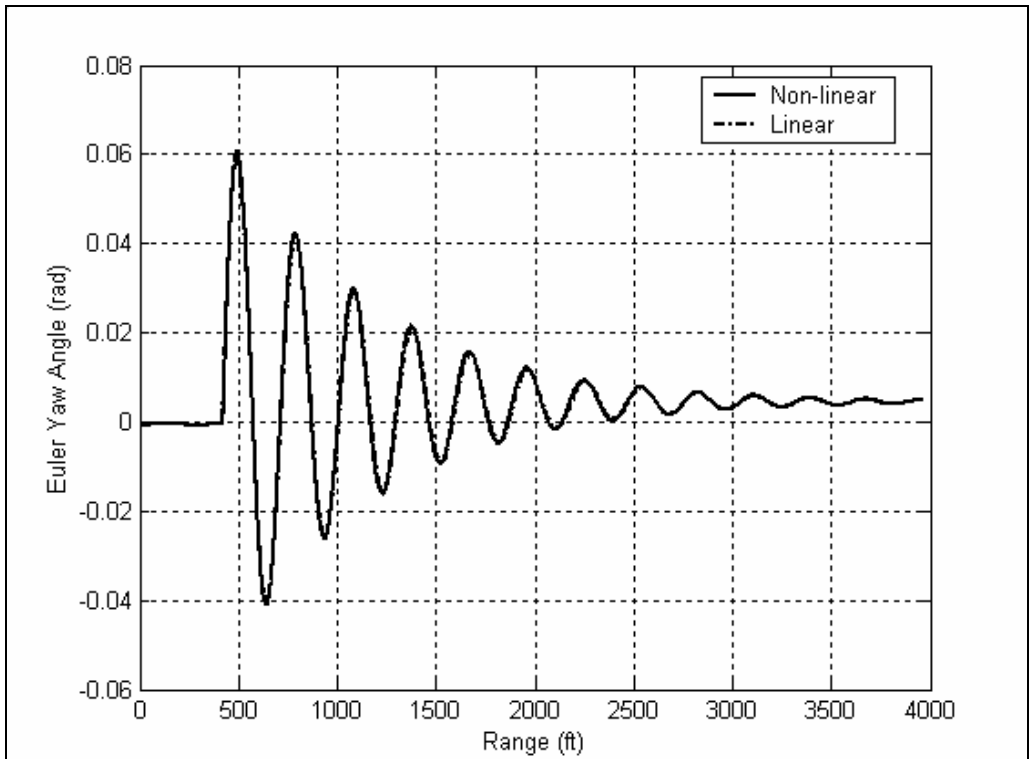


Figure 6. Yaw angle vs. range.

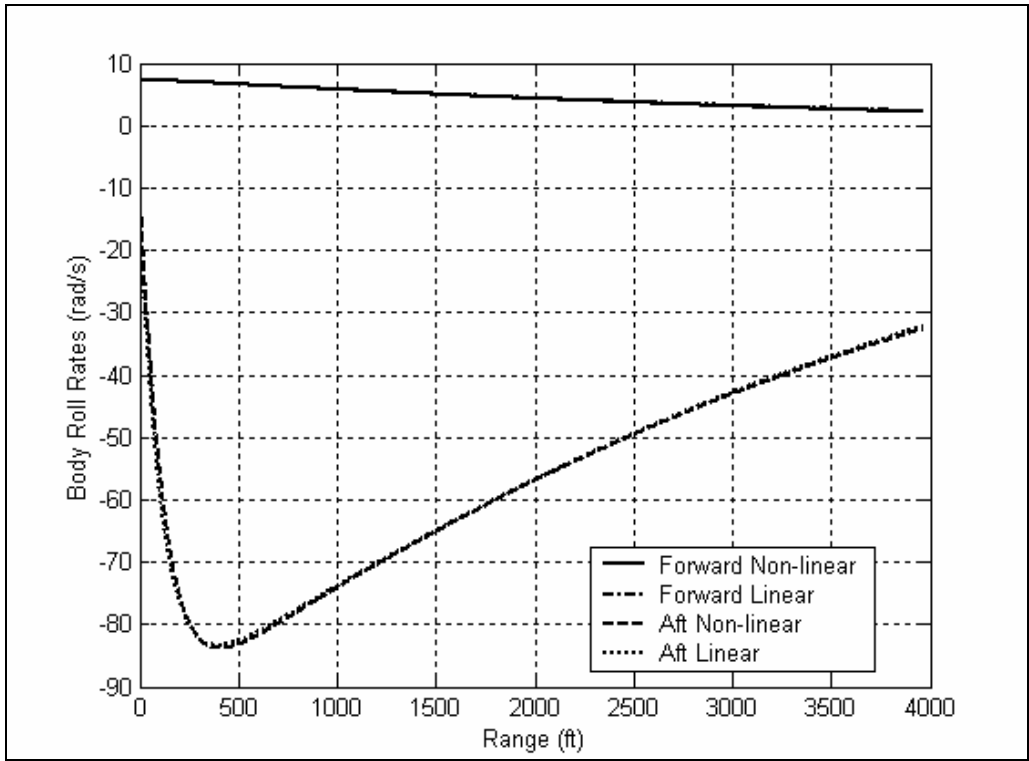


Figure 7. Roll rate vs. range.

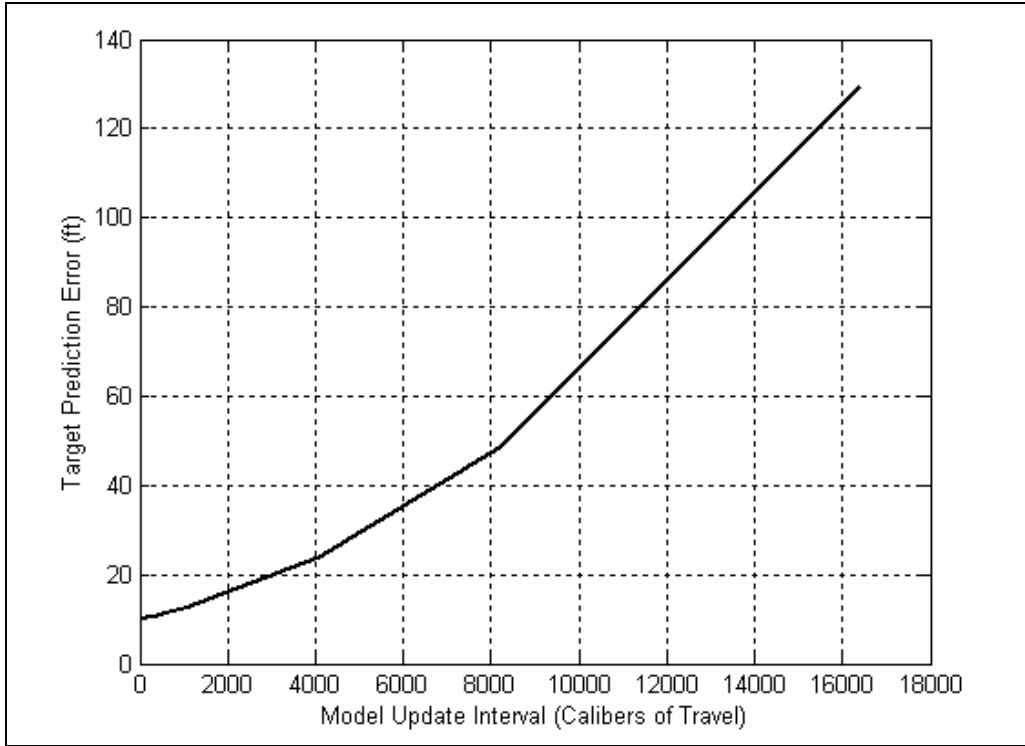


Figure 8. Target prediction error vs. model update interval.

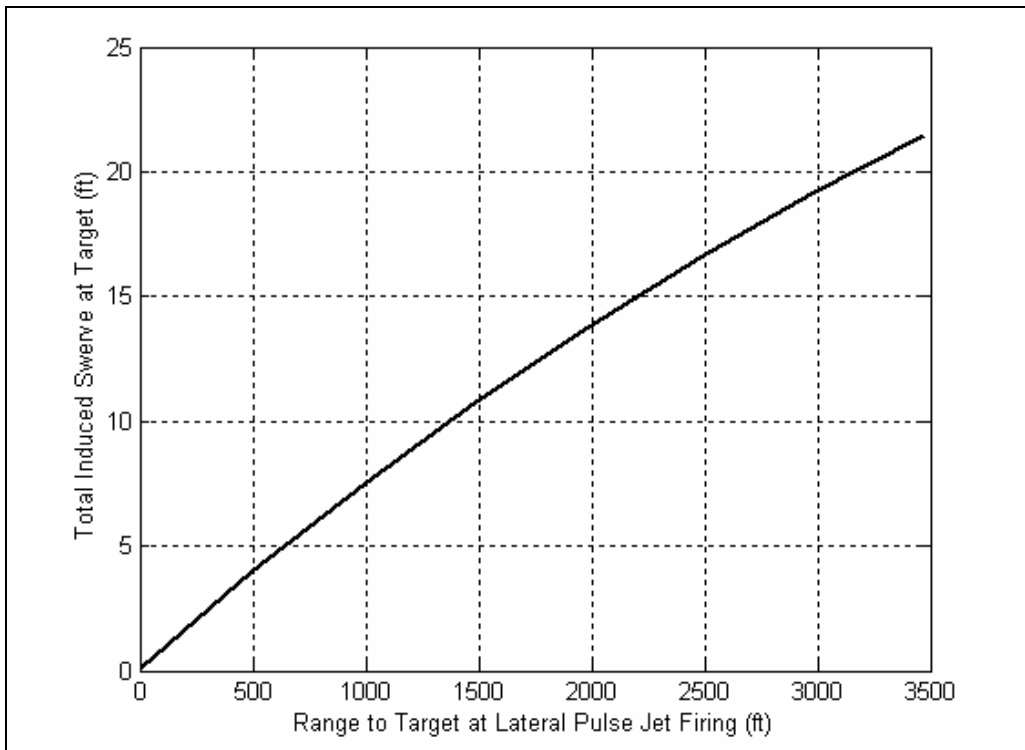


Figure 9. Induced pulsejet swerve vs. range to target.

6. Conclusions

A simple set of formulas has been developed for the swerve motion of a dual-spin projectile under the action of lateral pulsejets. The solutions provide a computationally low cost and reasonably accurate means of predicting impact points of a projectile that can be employed in future smart weapon flight control systems. For the best impact point prediction performance, the linear model that underlies the analytic solution must be periodically updated. For the example configuration examined here, the linear model should be updated no less than once per 4000 cal of range. The ability of lateral pulsejets to change the impact point steadily decreases with range to the target.

7. References

1. Guidos, B.; Cooper, G. Closed Form Solution of Finned Projectile Motion Subjected to a Simple In-Flight Lateral Impulse; Paper No. AIAA-2000-0767; *38th AIAA Aerospace Sciences Meeting and Exhibit*, Reno, NV, 2000.
2. Likins, P. W. Attitude Stability Criteria for Dual-Spin Spacecraft. *Journal of Spacecraft and Rockets* **1967**, *4*, pp 1638–1643.
3. Cloutier, G. J. Stable Rotation States of Dual-Spin Spacecraft. *Journal of Spacecraft and Rockets* **1968**, *5*, pp 490–492.
4. Mingori, D. L. Effects of Energy Dissipation on the Attitude Stability of Dual Spin Satellites. *AIAA Journal* **1969**, *7*, pp 20–27.
5. Fang, B. T. Energy Considerations for Attitude Stability of Dual-Spin Spacecraft. *Journal of Spacecraft and Rockets* **1968**, *5*, pp 1241–1243.
6. Hall, C. D.; Rand, R. H. Spinup Dynamics of Axial Dual-Spin Spacecraft. *Journal of Guidance, Control, and Dynamics* **1994**, *17*, pp 30–37.
7. Or, A. C. Resonances in the Despin Dynamics of Dual-Spin Spacecraft. *Journal of Guidance, Control, and Dynamics* **1991**, *14*, pp 321–329.
8. Cochran, J. E.; Shu, P. H.; Rew, S. D. Attitude Motion of Asymmetric Dual-Spin Spacecraft. *Journal of Guidance, Control, and Dynamics* **1982**, *5*, pp 37–42.
9. Tsuchiya, K. Attitude Behavior of a Dual-Spin Spacecraft Composed of Asymmetric Bodies. *Journal of Guidance, Control, and Dynamics* **1979**, *2*, pp 328–333.
10. Yang, H. X. Method for Stability Analysis of Asymmetric Dual-Spin Spacecraft. *Journal of Guidance, Control, and Dynamics* **1989**, *12*, pp 123–125.
11. Viderman, Z.; Rimrott, F. P. J.; Cleghorn, W. L. Stability of an Asymmetric Dual-Spin Spacecraft with Flexible Platform. *Journal of Guidance, Control, and Dynamics* **1991**, *14*, pp 751–760.
12. Stabb, M. C.; Schlack, A. L. Pointing Accuracy of a Dual-Spin Satellite due to Torsional Appendage Vibrations. *Journal of Guidance, Control, and Dynamics* **1991**, *16*, pp 630–635.
13. Smith, J. A.; Smith, K. A.; Topliffe, R. *Feasibility Study for Application of Modular Guidance and Control Units to Existing ICM Projectiles*. ARLCD-CR-79001; U.S. Army Armament Research and Development Command: Picatinny Arsenal, Dover, NJ, 1978.

14. Costello, M.; Peterson, A. Linear Theory of a Dual-Spin Projectile in Atmospheric Flight. *Journal of Guidance, Control, and Dynamics* **2000**, 23.
15. McCoy, R. L. *Modern Exterior Ballistics*; Schiffer Publishing Ltd.: Atglen, PA, 1999.
16. Ginsberg, J. H. *Advanced Engineering Dynamics*; Cambridge University Press: New York, NY, 1995.

Appendix. Dual-Spin Linear Theory Coefficients

$$\Omega_{vF} = \sqrt{(2 \operatorname{Re}(\xi_1 \eta_1^T)_{*1} \chi)^2 + (2 \operatorname{Im}(\xi_1 \eta_1^T)_{*1} \chi)^2}. \quad (\text{A-1})$$

$$\Omega_{vS} = \sqrt{(2 \operatorname{Re}(\xi_2 \eta_2^T)_{*1} \chi)^2 + (2 \operatorname{Im}(\xi_2 \eta_2^T)_{*1} \chi)^2}. \quad (\text{A-2})$$

$$\Omega_{wF} = \sqrt{(2 \operatorname{Re}(\xi_1 \eta_1^T)_{*2} \chi)^2 + (2 \operatorname{Im}(\xi_1 \eta_1^T)_{*2} \chi)^2}. \quad (\text{A-3})$$

$$\Omega_{wS} = \sqrt{(2 \operatorname{Re}(\xi_2 \eta_2^T)_{*2} \chi)^2 + (2 \operatorname{Im}(\xi_2 \eta_2^T)_{*2} \chi)^2}. \quad (\text{A-4})$$

$$\Omega_{qF} = \sqrt{(2 \operatorname{Re}(\xi_1 \eta_1^T)_{*3} \chi)^2 + (2 \operatorname{Im}(\xi_1 \eta_1^T)_{*3} \chi)^2}. \quad (\text{A-5})$$

$$\Omega_{qS} = \sqrt{(2 \operatorname{Re}(\xi_2 \eta_2^T)_{*3} \chi)^2 + (2 \operatorname{Im}(\xi_2 \eta_2^T)_{*3} \chi)^2}. \quad (\text{A-6})$$

$$\Omega_{rF} = \sqrt{(2 \operatorname{Re}(\xi_1 \eta_1^T)_{*4} \chi)^2 + (2 \operatorname{Im}(\xi_1 \eta_1^T)_{*4} \chi)^2}. \quad (\text{A-7})$$

$$\Omega_{rS} = \sqrt{(2 \operatorname{Re}(\xi_2 \eta_2^T)_{*4} \chi)^2 + (2 \operatorname{Im}(\xi_2 \eta_2^T)_{*4} \chi)^2}. \quad (\text{A-8})$$

$$\theta_{vF} = \tan^{-1} \left(\frac{2 \operatorname{Re}(\xi_1 \eta_1^T)_{*1} \chi}{-2 \operatorname{Im}(\xi_1 \eta_1^T)_{*1} \chi} \right). \quad (\text{A-9})$$

$$\theta_{vS} = \tan^{-1} \left(\frac{2 \operatorname{Re}(\xi_2 \eta_2^T)_{*1} \chi}{-2 \operatorname{Im}(\xi_2 \eta_2^T)_{*1} \chi} \right). \quad (\text{A-10})$$

$$\theta_{wF} = \tan^{-1} \left(\frac{2 \operatorname{Re}(\xi_1 \eta_1^T)_{*2} \chi}{-2 \operatorname{Im}(\xi_1 \eta_1^T)_{*2} \chi} \right). \quad (\text{A-11})$$

$$\theta_{wS} = \tan^{-1} \left(\frac{2 \operatorname{Re}(\xi_2 \eta_2^T)_{*2} \chi}{-2 \operatorname{Im}(\xi_2 \eta_2^T)_{*2} \chi} \right). \quad (\text{A-12})$$

$$\theta_{qF} = \tan^{-1} \left(\frac{2 \operatorname{Re}(\xi_1 \eta_1^T)_{*3} \chi}{-2 \operatorname{Im}(\xi_1 \eta_1^T)_{*3} \chi} \right). \quad (\text{A-13})$$

$$\theta_{qS} = \tan^{-1} \left(\frac{2 \operatorname{Re}(\xi_2 \eta_2^T)_{*3} \chi}{-2 \operatorname{Im}(\xi_2 \eta_2^T)_{*3} \chi} \right). \quad (\text{A-14})$$

$$\theta_{rF} = \tan^{-1} \left(\frac{2 \operatorname{Re}(\xi_1 \eta_1^T)_{*4} \chi}{-2 \operatorname{Im}(\xi_1 \eta_1^T)_{*4} \chi} \right). \quad (\text{A-15})$$

$$\theta_{rS} = \tan^{-1} \left(\frac{2 \operatorname{Re}(\xi_2 \eta_2^T)_{*4} \chi}{-2 \operatorname{Im}(\xi_2 \eta_2^T)_{*4} \chi} \right). \quad (\text{A-16})$$

In equations A1–A16, the notation τ_{*j} denotes the j th row of the matrix τ .

List of Symbols, Abbreviations, and Acronyms

C_{X0}^F, C_{X0}^A	Zero yaw axial force aerodynamic coefficient for the forward and aft bodies.
C_{X2}^F, C_{X2}^A	Yaw angle squared axial force aerodynamic coefficient for the forward and aft bodies.
C_{NA}^F, C_{NA}^A	Normal force aerodynamic coefficient for the forward and aft bodies.
C_{NPA}^F, C_{NPA}^A	Magnus force aerodynamic coefficient for the forward and aft bodies.
C_{DD}^F, C_{DD}^A	Roll moment aerodynamic coefficient due to fin cant for the forward and aft bodies.
C_{LP}^F, C_{LP}^A	Roll damping moment aerodynamic coefficient for the forward and aft bodies.
C_{MQ}^F, C_{MQ}^A	Pitch rate damping moment aerodynamic coefficient for the forward and aft bodies.
C_V	Viscous damping coefficient for hydrodynamic bearing.
D	Projectile characteristic length.
g	Gravity constant.
I_{XX}^F, I_{YY}^F	Roll and pitch inertia of the forward body projectile section.
I_{XX}^A, I_{YY}^A	Roll and pitch inertia of the aft body projectile section.
m	Total projectile mass.
m_A	Aft body mass.
m_F	Forward body mass.
p_F	Roll axis component of the angular velocity vector of the forward body expressed in the fixed plane reference frame.
p_A	Roll axis component of the angular velocity vector of the aft body expressed in the fixed plane reference frame.
q, r	Components of the angular velocity vector of both the forward and aft bodies expressed in the fixed plane reference frame.
r_{fx}, r_{fy}, r_{fz}	Fixed plane components of vector from composite center of mass to forward body mass center.

r_{ax}, r_{ay}, r_{az}	Fixed plane components of vector from composite center of mass to aft body mass center.
R_{fx}, R_{fy}, R_{fz}	Fixed plane components of vector from forward body mass center to forward body center of pressure.
R_{ax}, R_{ay}, R_{az}	Fixed plane components of vector from aft body mass center to aft body center of pressure.
$\tilde{R}_{ax}, \tilde{R}_{ay}, \tilde{R}_{az}$	Fixed plane components of vector from aft body mass center to aft body Magnus center of pressure.
$\tilde{R}_{fx}, \tilde{R}_{fy}, \tilde{R}_{fz}$	Fixed plane components of vector from forward body mass center to forward body Magnus center of pressure.
R_{IX}, R_{IY}, R_{IZ}	Fixed plane components of vector from composite body mass center to the impulse application point.
s	Nondimensional projectile arc length.
x, y, z	Position vector components of the composite center of mass expressed in the inertial reference frame.
Y_I, Z_I	Pulsejet force components in projectile body axes.
u, v, w	Translation velocity components of the composite center of mass resolved in the fixed plane reference frame.
V	Magnitude of mass center velocity.
θ, ψ	Euler pitch, and yaw angles.
ϕ_F	Euler roll angle of the forward body.
ϕ_A	Euler roll angle of the aft body.

NO. OF
COPIES ORGANIZATION

1 DEFENSE TECHNICAL
(PDF INFORMATION CTR
ONLY) DTIC OCA
8725 JOHN J KINGMAN RD
STE 0944
FORT BELVOIR VA 22060-6218

1 US ARMY RSRCH DEV &
ENGRG CMD
SYSTEMS OF SYSTEMS
INTEGRATION
AMSRD SS T
6000 6TH ST STE 100
FORT BELVOIR VA 22060-5608

1 INST FOR ADVNCD TCHNLGY
THE UNIV OF TEXAS
AT AUSTIN
3925 W BRAKER LN
AUSTIN TX 78759-5316

1 DIRECTOR
US ARMY RESEARCH LAB
IMNE ALC IMS
2800 POWDER MILL RD
ADELPHI MD 20783-1197

3 DIRECTOR
US ARMY RESEARCH LAB
AMSRD ARL CI OK TL
2800 POWDER MILL RD
ADELPHI MD 20783-1197

3 DIRECTOR
US ARMY RESEARCH LAB
AMSRD ARL CS IS T
2800 POWDER MILL RD
ADELPHI MD 20783-1197

ABERDEEN PROVING GROUND

1 DIR USARL
AMSRD ARL CI OK TP (BLDG 4600)

INTENTIONALLY LEFT BLANK.